Nuclear Science and Techniques (2024) 35:141
https://doi.org/10.1007/s41365-024-01508-z

# Adhesion property of AlCrNbSiTi high-entropy alloy coating on zirconium: experimental and theoretical studies

Bao-Liang Zhang[1] · Wen-Guan Liu[2] · Meng-He Tu[1] · Can Fang[1] · Yan Liu[3] · Yu-Hui Wang[1] · Yong Hu[1] · Hui Wang[1]

Received: 9 January 2024 / Revised: 17 May 2024 / Accepted: 20 May 2024 / Published online: 7 August 2024


**Abstract**
Experimental scratch tests and first-principles calculations were used to investigate the adhesion property of AlCrNbSiTi high-entropy alloy (HEA) coatings on zirconium substrates. AlCrNbSiTi HEA and Cr coatings were deposited on Zr alloy substrates using multi-arc ion plating technology, and scratch tests were subsequently conducted to estimate the adhesion property of the coatings. The results indicated that Cr coatings had better adhesion strength than HEA coatings, and the HEA coatings showed brittleness. The special quasi-random structure approach was used to build HEA models, and Cr/Zr and HEA/Zr interface models were employed to investigate the cohesion between the coatings and Zr substrate using first-principles calculations. The calculated interface energies showed that the cohesion between the Cr coating and the Zr substrate was stronger than that of the HEA coating with Zr. In contrary to Al or Si in the HEA coating, Cr, Nb, and Ti atoms binded strongly with Zr substrate. Based on the calculated elastic constants, it was found that low Cr and high Al content decreased the mechanical performances of HEA coatings. Finally, this study demonstrated the utilization of a combined approach involving first-principles calculations and experimental studies for future HEA coating development.

**Keywords** High-entropy alloy coating · Cr coating · Adhesion property · Scratch test · First-principles calculation

## 1 Introduction

The main fuel assembly material for commercial light water reactors (LWRs), zirconium alloy, reacts strongly with high-temperature steam (i.e., rapid oxidation and hydrogen production) under the loss of coolant accident (LOCA) condition, adversely affecting the safety of LWRs. Since the Fukushima nuclear accident in Japan in 2011, many efforts have been made to develop accident tolerance fuel (ATF) [1–4]. A primary way for ATF cladding development is to deposit a protective coating on the Zr alloy cladding surface and to isolate it from high-temperature steam to avoid direct contact. Multiple coating materials with potential Zr cladding applications have been investigated, such as Cr [5–8], CrAl [9, 10], CrSi [11], and FeCrAl [12]. Owing to its high oxidation stability under hydrothermal corrosion conditions, high-temperature oxidation conditions, and good compatibility with Zr alloys, Cr coating has been chosen as the primary material for coated cladding development in engineering applications after a thorough technical exploration of almost ten years [13]. However, although Cr coating has good comprehensive properties, diffusion occurs at the interface between the Cr coating and Zr substrate to form the brittle phase of $ZrCr_2$ at high temperatures [14–16]. Therefore, new coatings are still need to be developed to further improve the protection performance in LWRs.

The high-entropy alloys (HEAs), proposed by Yeh [17], have gained significant attention owing to their potential advantages [18–24]. Coatings made of HEAs, i.e., HEA coatings, have also recently attracted extensive attention

This work was supported by Stability Supports Research Project of Treasury Department (No. 197801) and Talent Fund of CIAE (No. 219213).

✉ Bao-Liang Zhang
zhangbaoliang@yeah.net

✉ Wen-Guan Liu
liuwg7@mail.sysu.edu.cn

[1] China Institute of Atomic Energy, Beijing 102413, China

[2] Sino-French Institute of Nuclear Engineering and Technology, Sun Yat-Sen University, Zhuhai 519082, China

[3] School of Power and Mechanical Engineering, Wuhan University, Wuhan 430072, China

because of their various technologically favorable properties. First, HEA coatings have excellent mechanical properties [25–27], thermal stability [28], and corrosion resistance [29, 30]. Second, HEA coating performance optimization can be achieved by composition design [31–35]. The adjustability of elements in HEAs present significant opportunities for the improvement of their coating performance. In recent years, research has been focused to develop HEA coatings as viable coating materials for ATF. Various HEAs, such as AlCrMoNbZr HEA [36–38], AlNbTiZr medium-entropy alloys [30, 35], and amorphous multi-component FeCrAlMoSiY alloys [39, 40], have been deposited on Zr alloys, and their performance has been evaluated.

Now, it is of primary importance that the elements to be used for cladding should have a low thermal neutron absorption cross section and are not easily activated in the reactor environment. The thermal neutron absorption cross sections of Al, Cr, Nb, Si, and Ti are 0.23, 3.05, 1.15, 0.17, and 6.09 barn, respectively, which are relatively low as compared with other elements. Thus, considering the thermal neutron absorption cross sections of these elements and their oxidation resistance to high-temperature steam, AlCrNbSiTi HEA coating was designed as a protective coating for the Zr alloy in this study. The service performance of AlCrNbSiTi HEA coatings, such as high-temperature steam oxidation resistance [41], and fretting corrosion performance [42] were also examined. It is known that the adhesion between the coating and Zr substrate is a critical fundamental property for applications. Hence, the study of the adhesion property of AlCrNbSiTi HEA coatings was focused herein using both experimental and theoretical methods. Cr coating was used as the contrast coating material owing to its present wide applicability as the ATF cladding coating.

## 2 Research methods

### 2.1 Experimental methods

The Cr and AlCrNbSiTi HEA coatings were deposited on Zr-Sn-Nb alloy substrates (20 mm × 20 mm × 0.6 mm) using multi-arc ion plating technology. Three targets of the pure Ti (99.99%), pure Cr (99.99%), and $Al_{34}Cr_{22}Nb_{11}Si_{11}Ti_{22}$ alloy were used in the deposition process. Prior to deposition, the Zr alloy substrates were initially hand-polished with 2000 grit sandpaper, cleaned ultrasonically in acetone followed by ethanol to remove surface contaminants, and heated further to remove moisture. The deposition chamber was heated to 300 °C to remove the water vapor and evacuated to a base pressure below $6 \times 10^{-4}$ Pa. Subsequently, the substrate surfaces were etched using an arc-enhanced glow discharge (AEGD) process to remove contaminants (such as surface oxides) and to increase surface roughness. Cr and AlCrNbSiTi HEA coatings (of approximately 10 µm thickness) were then deposited individually on the substrates. The detailed deposition parameters are listed in Table 1.

The surface and cross-section morphology of the Cr and AlCrNbSiTi HEA coatings on the Zr alloy substrates were examined using a scanning electron microscope (SEM, Phenom XL). The samples for cross-section SEM were cut, sanded, and polished (finally with a 0.05 µm $Al_2O_3$ water-based suspension). The fine structures and chemical compositions of the coatings were investigated using a transmission electron microscope (TEM, Talos F200X). TEM samples were prepared using a focused ion beam (FIB, Scios 2 DualBeam). The crystal structures of the coatings were studied using a grazing incident X-ray diffractometer (GIXRD, X'Pert MRD). The grazing incidence angle was 1°, and the diffraction scan range was $10° < 2\theta < 90°$, with a step size of 0.02°.

The interface adhesion strength of the Cr and AlCrNbSiTi HEA coatings was tested using an automatic scratch tester (CASSTeP500_NHT3_MCT3) with a diamond ball cone indenter (apex angle was 120° ± 1.0°, and its radius ($R$) was 100 µm ± 10%). Scratch tests were made under a stepwise linearly increasing load (applied from 0N to 10N, 30N) over the scratch length (2000 µm), and the corresponding scratch SEM morphology, friction (Ft), acoustical emission signal (AE), penetration depth (Pd), normal load (YFn), and friction coefficient (µ) images were recorded and subsequently analyzed.

### 2.2 Computational methods

First-principles calculations can provide an in-depth explanation of the origin of the coating performance [43, 44] and play a key role in predicting HEA coating performance [45].

**Table 1** Deposition parameters of the Cr and AlCrNbSiTi HEA coatings

| Process and obtained coating | Bias voltage (V) | Gas/Pressure (Pa) | Target/current or power | Duration (min) |
|---|---|---|---|---|
| AEGD process | −150 | Ar/0.5 | Ti/100 A | 30 |
| Cr coating | −50 | Ar/0.5 | Cr/100 A | 60 |
| AlCrNbSiTi HEA coating | −50 | Ar/0.5 | $Al_{34}Cr_{22}Nb_{11}Si_{11}Ti_{22}$ /600W | 60 |

Additionally, these calculations can explain the structure strength and other properties from the atomic or electronic level [43, 44, 46, 47], to supplement the experimental findings.

The special quasi-random structure (SQS) [48] approach was used to build the AlCrNbSiTi HEA models, and the mcsqs code from the alloy-theoretic automated toolkit (ATAT) [49] was utilized to generate the SQS models. The first and second nearest-neighbor pairs were optimized to ensure close proximity to the ideal mixing state. The SQS models were also screened according to Born's dynamical stability criteria [50]. Figure 1 shows the unrelaxed SQS models of HEA crystal structures with different alloy compositions, where the SQS model with FCC structure has 32 atoms. Based on the HEA SQS models, a series of HEA(111)/ Zr(0001) interfaces were built, one of which is shown in Fig. 2b. Figure 2a also shows the Cr(110)/Zr(0001) interface model. As shown in Fig. 2, the two Zr layers closest to the interface are denoted as Zr-1 and Zr-2, and the two coating atomic layers closest to the interface are labeled as Coating-1 and Coating-2. A, B, and C in Fig. 2 are the assumed fracture planes.

The Vienna ab initio simulation package (VASP) [51] was employed to perform electronic state calculations within the density functional theory (DFT) [52, 53]. Electron-ion interactions were described by the projector-augmented plane-wave (PAW) [54] method, and the wave functions were expanded in a plane-wave basis set with a cutoff energy of 280 eV. A generalized gradient approximation (GGA) [55] of the exchange correlation energy was used in the PBE scheme. The total energy and Hellmann–Feynman forces were convergent within $10^{-5}$ eV and $10^{-2}$ eV/Å, respectively. The Monkhorst–Pack k-point meshes of $7 \times 4 \times 1$ and $3 \times 3 \times 1$ were used to sample the Brillouin zone [56] for the supercells of Cr/Zr and HEA/Zr interfaces, respectively. Ab initio molecular dynamics (AIMD) simulations were also conducted to obtain the amorphous HEA structures. The HEA structures were subjected to pre-melting, melting, and then quenching to 0K to induce amorphicity. The FCC-structured HEA was used solely to build the amorphous high-entropy alloy, and it was observed that this composition would not form an FCC structure. However, for comparison with amorphous structures, the FCC-structured HEA was also investigated in this study.

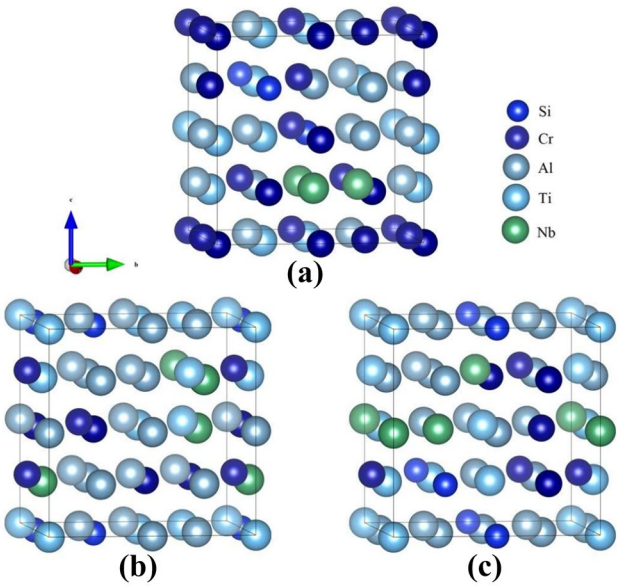


**Fig. 1** (Color online) Unrelaxed SQS models of HEA alloy crystal structures: **a** $Al_{11}Cr_9Nb_3Si_2Ti_7$, **b** $Al_{13}Cr_7Nb_3Si_2Ti_7$, and **c** $Al_{15}Cr_5Nb_3Si_2Ti_7$

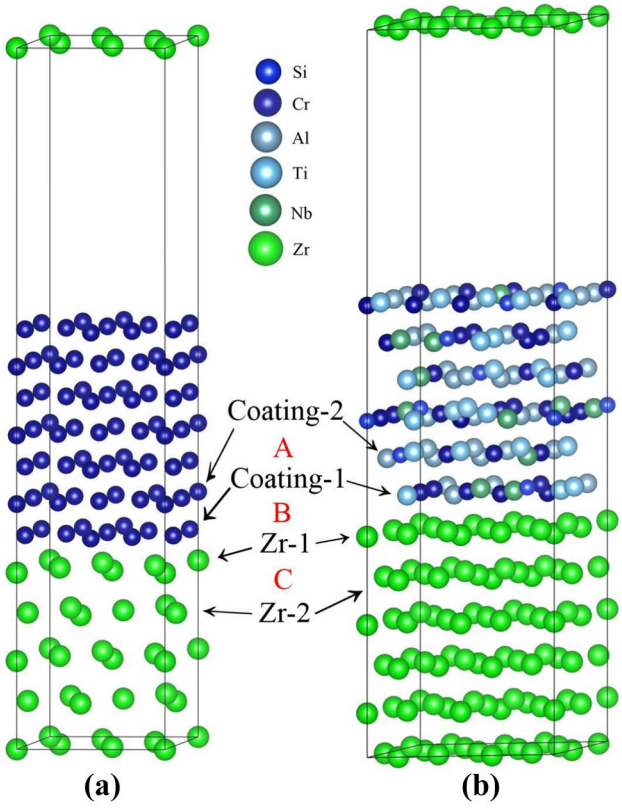


**Fig. 2** (Color online) The unrelaxed models of **a** Cr/Zr and **b** FCC HEA/Zr interfaces. Zr-1 and Zr-2 indicate the atomic layers closest to the Zr substrate interface, and Coating-1 and Coating-2 denote the atomic layers closest to the Cr and HEA coatings interface. A, B, and C represent the different fracture planes between these atomic layers

## 3 Results and discussion

### 3.1 Coating microstructure and adhesion strength

Figure 3a, c shows the surface SEM images of the Cr and AlCrNbSiTi HEA coatings, respectively. Both coatings

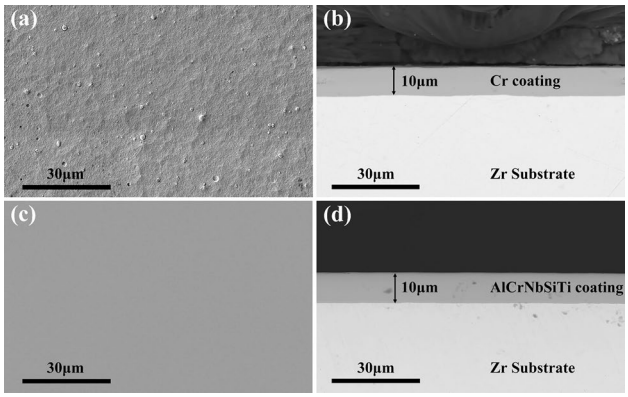


**Fig. 3** (Color online) Surface and cross-sectional SEM images of the coatings: **a** Cr coating surface, **b** Cr coating cross-sectional, **c** AlCrNbSiTi HEA coating surface, and **d** AlCrNbSiTi HEA coating cross-sectional

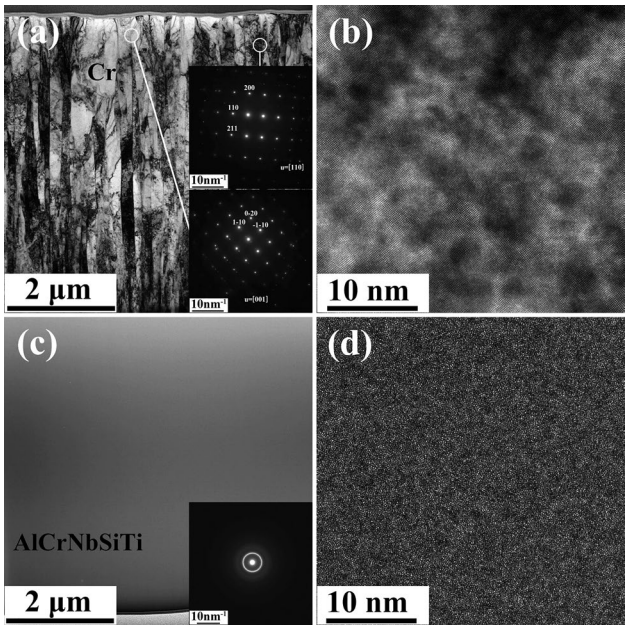


**Fig. 4** TEM images of coatings: **a** Cr coating, **b** HRTEM of Cr coating, **c** AlCrNbSiTi HEA coating, and **d** HRTEM of AlCrNbSiTi HEA coating

exhibited a smooth cracks-free surface morphology. Droplets and voids (μm scale) were distributed on the Cr coating surface, generally formed during multi-arc ion plating [57]. On the contrary, the AlCrNbSiTi HEA coating exhibited a smoother surface. Figure 3b, d shows the cross-sectional SEM images of the Cr and AlCrNbSiTi HEA coatings, respectively. Both coatings had a uniform thickness of approximately 10 μm with no defects (such as delamination, holes, or cracks) found between coatings with the Zr substrate, indicating a good quality deposition well-adhered to the Zr substrate.

Figure 4a shows the TEM images of the Cr coating. The Cr coating microstructure exhibited a typical columnar crystal structure, and the grain width of the columnar crystal was approximately 0.3 μm. The diffraction patterns along the [110] and [001] strip axes demonstrated typical BCC characteristics [57], as shown in Fig. 4a. The high-resolution TEM (HRTEM) of the Cr coating is shown in Fig. 4b, with a clearly visible crystal structure. Figure 4c shows the TEM image of the AlCrNbSiTi HEA coating. No obvious discernible microstructure was observed in the coating. The diffraction pattern of the AlCrNbSiTi HEA coating showed a typical amorphous structure characteristic, as shown in Fig. 4c. The HRTEM of the AlCrNbSiTi HEA coating is shown in Fig. 4d, where an obvious chaotic atomic structure was observed. Thus, from Fig. 4c, d, it can be verified that the AlCrNbSiTi HEA coating deposited on the Zr alloy substrate is an amorphous structure. Furthermore, an energy-dispersive X-ray spectrometry (EDS) composition analysis of the AlCrNbSiTi HEA coating was performed. The peaks of Al, Cr, Nb, Si, and Ti were detected. All the elemental compositions—Al: 35.9, Cr: 21.1, Nb: 11.6, Si: 11.4, and Ti: 20.0 at.%—calculated by averaging over four data points were found to be agreeing with the $Al_{34}Cr_{22}Nb_{11}Si_{11}Ti_{22}$ target alloy composition, indicating a good coating deposition process.

Figure 5 shows the GIXRD patterns of the Cr and AlCrNbSiTi HEA coatings, and the Zr substrate. The peaks of Zr, such as (002) and (103), in the top pattern (blue curve) were obvious. Most Cr coating peaks, in the bottom pattern (black curve), were similar to the Zr peaks, except for one extremely strong peak in the 64.6° position from Cr (200). The AlCrNbSiTi HEA coating peaks, in the middle pattern (red curve), were extremely similar to those of the

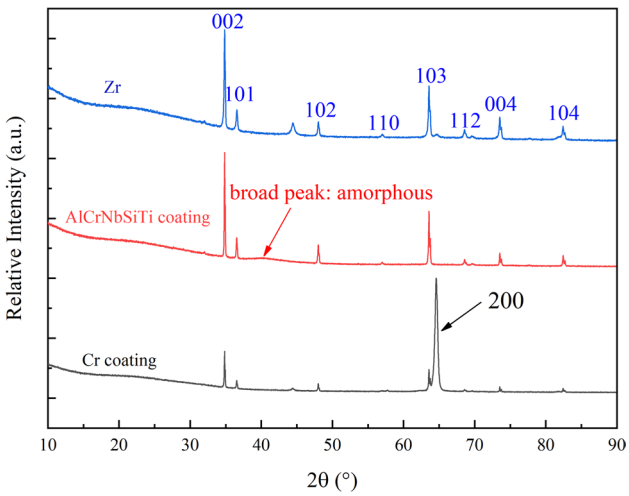


**Fig. 5** (Color online) GIXRD patterns of the Cr coating, AlCrNbSiTi HEA coating, and Zr substrate

Zr, and no obvious new peaks appeared. Notably, a broad peak appeared (between ~38°-~45°) after the Zr (101) peak, indicating the amorphous nature of AlCrNbSiTi HEA coating, in agreement with the TEM results.

Figure 6a and b shows the scratch SEM morphology, Ft, AE, Pd, YFn, and μ images of the Cr and AlCrNbSiTi HEA coatings under 0–30 N normal load, respectively. As shown in Fig. 6a, the Cr coating scratch was relatively flat with no obvious spalling, which indicated good adhesion between the Cr coating and Zr substrate. However, it is worth noting that once the scratch length exceeded 950 μm, cracks appeared on the scratch surface successively, corresponding to penetration depth (Pd) > 10 μm (the thickness of the coating). The friction (Ft) curve (black line in Fig. 6a) increased almost linearly to ~ 15 N. The curve of friction coefficient (μ, the light blue line in Fig. 6a) increased rapidly to ~ 0.2, and then gradually reached a slower increase to 0.5. The acoustic emission signal (AE) curve (red line in Fig. 6a) initially appeared stable at ~ 2% (corresponding scratch length 0–380 μm), and then showed a wavy increasing trend to ~ 14% (corresponding to scratch length 380–2000 μm). The AE wave peaks that appeared after the scratch length > 950 μm corresponded to the cracks in the SEM morphology. The Pd curve (green line in Fig. 6a) appeared to be linear increasing with the maximum scratch depth ~ 23 μm, except for a bump after Pd ~ 11 μm corresponding to scratch length 920–1000 μm, YFn ~ 13N and a wave increase of AE from 4.5–9.5% which most likely occurred owing to the indenter reaching the interface between the Cr coating and Zr substrate.

The scratch on the AlCrNbSiTi HEA coating showed a significant difference with the Cr coating, shown in Fig. 6b. Although the scratch initially appeared relatively flat (corresponding scratch length 0–320 μm), cracks similar to the Cr coating in Fig. 6a also appeared. Obvious spalling (brittle cracking similar to ceramics) was observed once the scratch

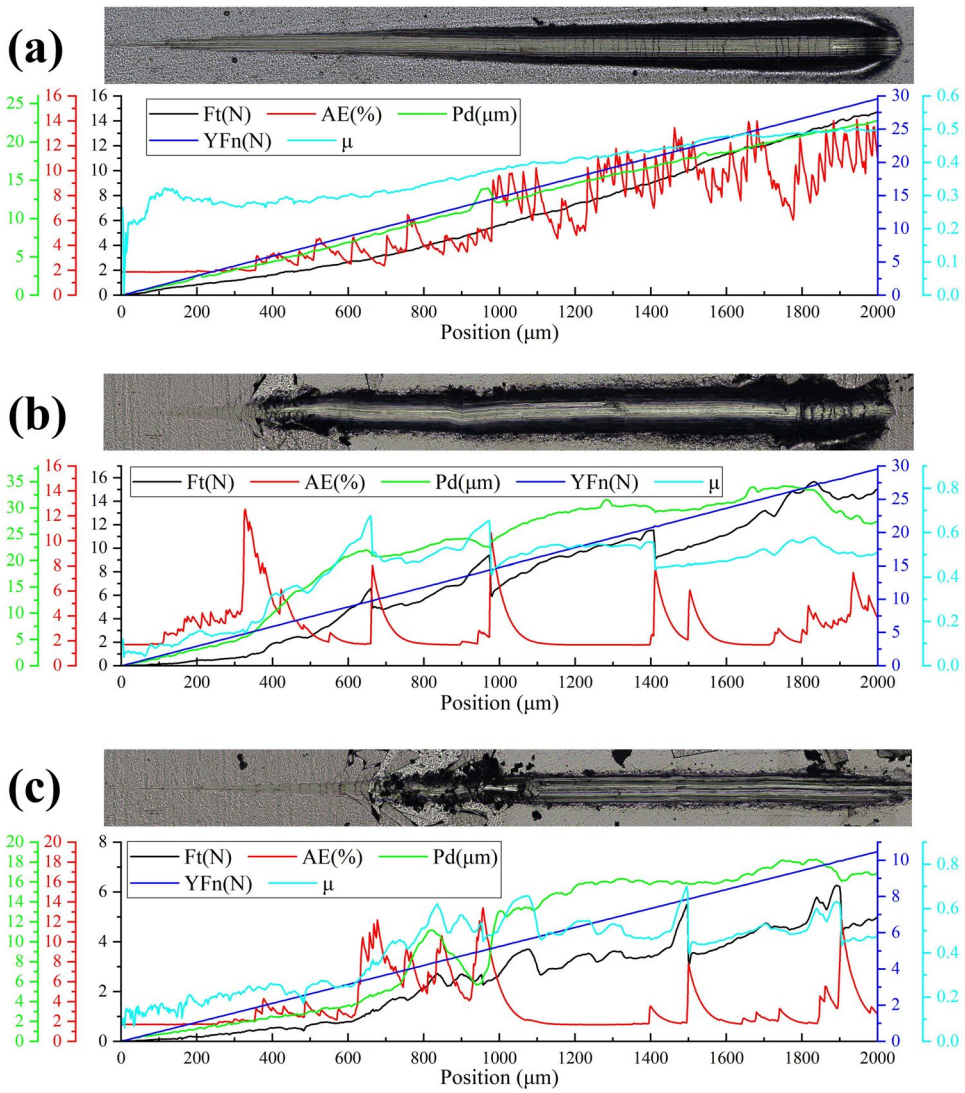


**Fig. 6** (Color online) Scratch SEM morphology and other coating information: **a** Cr coating under 0–30 N, **b** AlCrNbSiTi HEA coating under 0–30 N, and **c** AlCrNbSiTi HEA coating under 0–10 N. Ft represents friction, AE represents acoustical emission signal, Pd represents penetration depth, YFn represents normal load, and μ represents friction coefficient

length exceeded 320 µm (corresponding YFn > 5N), which indicated relatively poor adhesion between the AlCrNbSiTi coating and Zr substrate. The first large wave (increases rapidly from ~ 5 to 13%) in the AE curve (red line in Fig. 6b) corresponds to the first spalling in the SEM morphology; subsequent waves in the AE curve suggest multiple brittle spalling. A significant increase in the Ft curve (black line in Fig. 6b), µ curve (light blue line in Fig. 6b), and Pd curve (green line in Fig. 6b) also corresponded to each spalling. To clearly obtain the coating breaking process, a scratch under 0–10 N normal load was also made for the AlCrNbSiTi HEA coatings (shown in Fig. 6c). The scratch results were similar to Fig. 6b, more visible cracking and spalling was observed, which also indicated the brittle AlCrNbSiTi HEA coating property and relatively poor adhesion between the AlCrNbSiTi HEA coating and Zr substrate.

### 3.2 First-principles calculation

Table 2 lists the calculated lattice constants for BCC Cr and FCC HEA. The calculated lattice constant of Cr is found to be in good agreement with the experimental result [58]. As the Al content increased and Cr content decreased in HEA alloys, the HEA lattice constant increased from 7.792–7.910 Å as shown in Table 3. This is because the atomic size of Al is larger than that of Cr. To determine the adhesion between the coatings and Zr substrate, the interface energy, $E_{\text{interface}}$, is calculated as follows:

$$E_{\text{interface}} = E_{\text{total}} - E_{\text{coating}} - E_{\text{Zr}}, \quad (1)$$

where $E_{\text{total}}$, $E_{\text{coating}}$, $E_{\text{Zr}}$ are the calculated energies of the interface supercell, the coating, and the Zr substrate, respectively. A negative value indicates strong cohesion between the coatings and Zr substrate. Table 3 shows that the cohesion between the Cr/Zr interface is stronger than those between FCC HEA/Zr and amorphous HEA/Zr interfaces. Comparing the two HEA coatings, the cohesion strength is not affected by the FCC and amorphous structures of HEA. Moreover, the composition of $Al_{11}Cr_9Nb_3Si_2Ti_7$ was further examined to explore the cohesion mechanism between the HEA coatings and Zr substrate in the following sections.

**Table 2** Calculated lattice constants for BCC Cr and FCC HEA, alongside experimental result for Cr

| Compositions | This work (Å) | Exp. (Å) |
|---|---|---|
| BCC Cr | 2.837 | 2.884 [58] |
| FCC $Al_{11}Cr_9Nb_3Si_2Ti_7$ | 7.792 | – |
| FCC $Al_{13}Cr_7Nb_3Si_2Ti_7$ | 7.853 | – |
| FCC $Al_{15}Cr_5Nb_3Si_2Ti_7$ | 7.910 | – |

**Table 3** Calculated interface energies (eV/Å$^2$) for Cr/Zr interface and mean binding energies between Zr substrate and different HEA coatings

| Compositions | Structure | Interface energy |
|---|---|---|
| Cr | BCC | −0.26 |
| $Al_{11}Cr_9Nb_3Si_2Ti_7$ | FCC | −0.22 |
| $Al_{13}Cr_7Nb_3Si_2Ti_7$ | FCC | −0.21 |
| $Al_{15}Cr_5Nb_3Si_2Ti_7$ | FCC | −0.21 |
| $Al_{11}Cr_9Nb_3Si_2Ti_7$ | amorphous | −0.22 |
| $Al_{13}Cr_7Nb_3Si_2Ti_7$ | amorphous | −0.24 |
| $Al_{15}Cr_5Nb_3Si_2Ti_7$ | amorphous | −0.22 |

To further investigate the cohesion between the coatings and Zr substrate, first-principles tensile tests were performed. A uniaxial tensile strain with a 2% increment in the interface normal direction was applied. In each strain step, the starting atomic configuration was obtained from the relaxed configuration of the preceding step. Figure 6 shows the result of the first-principles tensile test for the Cr/Zr interface. The maximum strength was 9.9 GPa at a strain of 12%. However, at 14% strain, the interface broke up between the layers Zr-1 and Zr-2. C is the final fracture plane as shown in the inset of Fig. 7. The Cr/Zr interface did not break along the A or B plane in Fig. 2. This means that the bonding strength across the C plane (i.e., bonds between Zr-1 and Zr-2 layers) determines the cohesion strength of Cr/Zr interface.

To confirm the results in Fig. 7, first-principles tensile tests using a rigid separation method were performed. For the rigid separation method, the interface structures were separated at different planes (i.e., the A, B, and C planes in

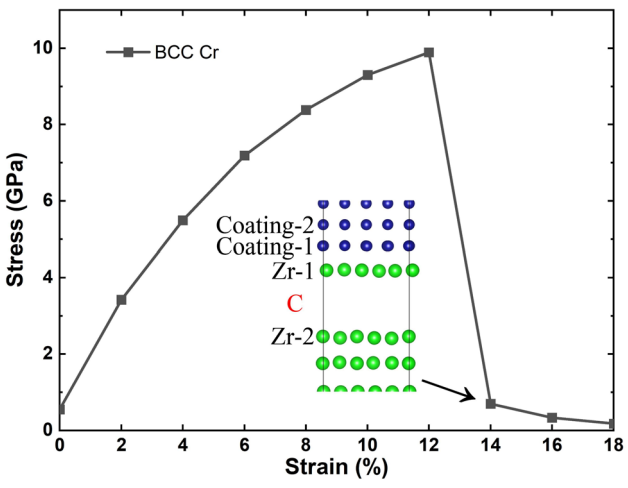


**Fig. 7** (Color online) First-principles tensile test for Cr/Zr interface. The inset represents the atomic structure after the Cr/Zr interface breakup

Fig. 2) with an increment of 0.1 Å in the interface normal direction; however, the atomic structures on both sides of the fracture plane were not relaxed. The results for the Cr/Zr interface are shown in Fig. 8 and Table 4. In Fig. 8, the separation energy for fracture plane A was consistently higher than those of the B and C planes during the tensile test. In Table 4, the maximum separation energy for the A plane was 0.48 eV/Å$^2$, and those for the B and C planes were only 0.26 eV/Å$^2$ and 0.21 eV/Å$^2$, respectively. Thus, it was most difficult to separate the interface structure at the A plane, meaning that the Cr–Cr bonds across the A plane are significantly stronger than the Cr–Zr bonds across the B plane and the Zr–Zr bonds across the C plane. As a result, the Cr/Zr interface breaks at the C plane preferentially, which is in good agreement with the results shown in Fig. 7.

Figures 7 and 8 show that first-principles tensile tests have achieved identical results with and without the rigid separation method. Further, first-principles tensile tests with the rigid separation method have lower computational cost and can be used to calculate the separation energies for different fracture planes. Hence, this method was further used to identify the cohesion strength between the HEA coating and Zr substrate, and the results are shown in Fig. 9 and Table 4. The HEA coatings with both FCC and amorphous structures were both studied. In Fig. 9, for each fracture plane, the separation energies for FCC and amorphous HEAs have the similar values. The separation energy is listed in the following order: FCC/amorphous HEA-A > FCC/amorphous HEA-B > FCC/amorphous HEA-C. Therefore, the Zr–Zr bonding across the C plane is the weakest with the separation energy of 0.20 eV/Å$^2$ in Table 4, and the breakage would occur at the C plane of

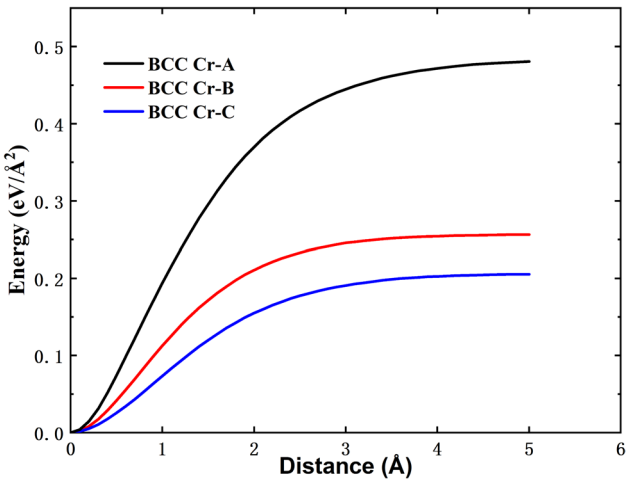


**Fig. 8** (Color online) Change tendency of separation energy eV/Å$^2$ during first-principles tensile test using rigid separation method for the Cr/Zr interface with respect to unseparated models. A, B, and C denote different fracture planes as shown in Fig. 2

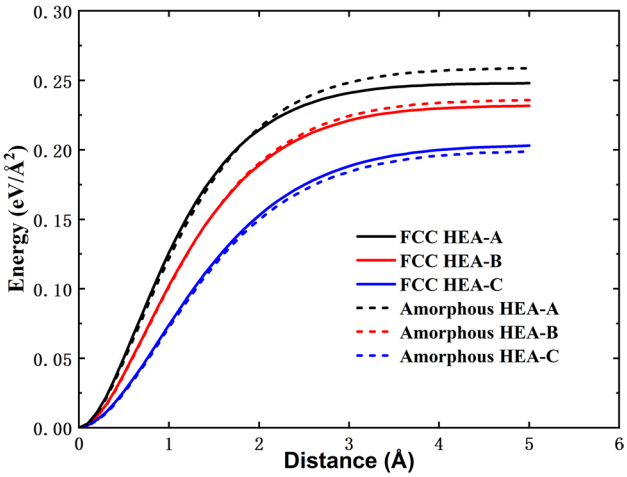


**Fig. 9** (Color online) Change tendency of separation energy eV/Å$^2$ during first-principles tensile test using rigid separation method for FCC HEA/Zr and amorphous HEA/Zr interfaces with respect to unseparated models. A, B, and C denote different fracture planes as shown in Fig. 2

the FCC HEA/Zr and amorphous HEA/Zr interfaces. This is in good agreement with the results of the Cr/Zr interface in Fig. 8.

Table 4 shows that the Cr–Cr bonding across the A plane of the Cr/Zr interface, with the separation energy of 0.48 eV/Å$^2$, is significantly stronger than the bonding across the A plane of the HEA/Zr interfaces. For the B plane, the Cr–Zr bonding in the Cr/Zr interface, with 0.26 eV/Å$^2$, is also stronger than the bonding between HEA and Zr atoms in the HEA/Zr interfaces. However, the bonding across the C plane is the Zr–Zr bonds for all interfaces, i.e., the bonds between Zr-1 and Zr-2 layers in Fig. 2, which results in similar separation energies as shown in Table 4.

To determine the underlaying mechanism in the cohesion of different interfaces, the charge densities for the Cr/Zr, FCC HEA/Zr, and amorphous HEA/Zr interfaces were investigated and are shown in Fig. 10. As demonstrated in Fig. 10, the charge densities in Cr and HEA coatings are significantly denser than those in the Zr substrate, and the charge densities in the amorphous HEA coating are random in Fig. 10c compared with those in Figs. 10a and b. It can be

**Table 4** Calculated maximum separation energies per area (eV/Å$^2$) for Cr/Zr and HEA/Zr interfaces by rigid separation method in Figs. 4 and 5

| Compositions | Structure | A | B | C |
|---|---|---|---|---|
| Cr | BCC | 0.48 | 0.26 | 0.21 |
| HEA alloy | FCC | 0.25 | 0.23 | 0.20 |
| | amorphous | 0.26 | 0.24 | 0.20 |

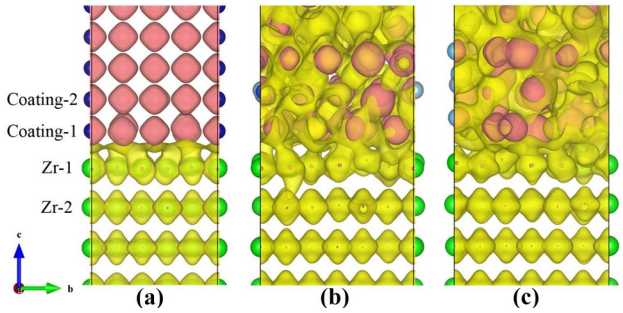


**Fig. 10** (Color online) Charge densities for **a** Cr/Zr, **b** FCC HEA/Zr, and **c** amorphous HEA/Zr interfaces. The yellow and red isosurfaces indicate 0.03 and 0.06 electrons/Bohr$^3$, respectively

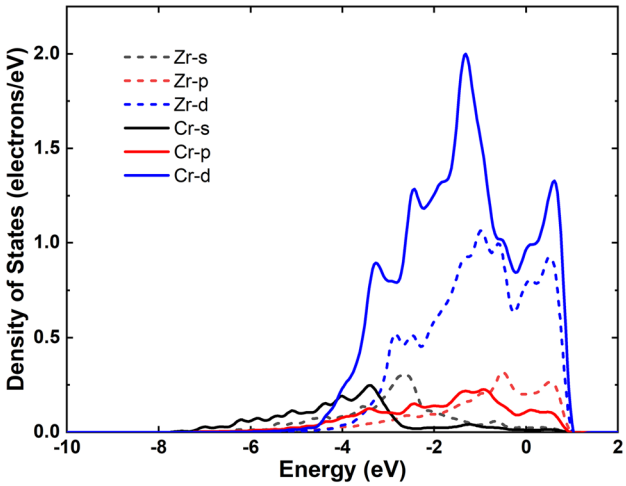


**Fig. 11** (Color online) Density of states (electrons/eV) for Zr and Cr atoms in the Cr/Zr interface in Fig. 2a

observed that the charge densities between Zr-1 and Coating-1 atoms are higher than those between Zr-1 and Zr-2 atoms. This indicates that the bonding between the Zr-1 and Zr-2 layers is weaker and will preferentially break, which is in good agreement with the results of first-principles tensile test.

Furthermore, the density of states for atoms in the Zr-1 and Coating-1 layers of the Cr/Zr and FCC HEA/Zr interfaces were calculated and are shown in Figs. 11 and 12, respectively. In Fig. 11, the density of states of Cr overlaps with that of Zr. Specifically, many hybridization peaks exist between the Cr-d and Zr-d electrons, indicating a relatively strong bonding between Cr and Zr. This confirms the results in Table 4 and Fig. 10. Similarly, in Fig. 12b and d, an obvious overlap emerges between the density of states of Nb/Ti and Zr atoms with the existence of many hybridization peaks. However, in Fig. 12a and c, no hybridization peaks are evident between Al/Si and Zr atoms, indicating a relatively weak bonding between Al/Si and Zr atoms. Hence, for the HEA coating, Cr, Nb, and Ti atoms form a stronger bonding with the Zr substrate than Al and Si atoms, and the cohesion between the HEA coating and Zr substrate is weaker than that between the Cr coating and Zr substrate, which also confirms the results shown in Table 4 and Fig. 10. Thus, reducing Al concentration improves the interface adhesion to a certain extent.

To investigate the mechanical properties of Cr, FCC HEA, and amorphous HEA coatings, the elastic constants were calculated. Because the chemical distribution in HEA SQS supercells can result in an anisotropic structure and scatter the elastic constants, an averaging approach [59] was applied to obtain the values of $C_{11}$, $C_{12}$, and $C_{44}$ as follows:

$$C_{11} = (c_{11} + c_{22} + c_{33})/3, \tag{2}$$

$$C_{12} = (c_{12} + c_{23} + c_{13})/3, \tag{3}$$

$$C_{44} = (c_{44} + c_{55} + c_{66})/3, \tag{4}$$

Using these average values, bulk modulus $B$, shear modulus $G$ [60, 61], Young's modulus $E$, and Cauchy pressure ($\Gamma$) were calculated as follows:

$$B = (c_{11} + 2c_{12})/3, \tag{5}$$

$$G = (G_V + G_R)/2, \tag{6}$$

$$G_V = (C_{11} - C_{12} + 3C_{44})/5, \tag{7}$$

$$G_R = [5(C_{11} - C_{12})C_{44}]/[3(C_{11} - C_{12}) + 4C_{44}], \tag{8}$$

$$E = 9BG/(3B + G), \tag{9}$$

$$\Gamma = C_{11} - C_{44}, \tag{10}$$

AIMD simulations were conducted to obtain the amorphous HEA structures with random structures in Fig. 13, investigated using the averaging approach.

The calculated elastic moduli ($B$,$G$ and $E$), Pugh's ratio $B/G$, and Cauchy pressure ($\Gamma$) for the Cr and HEA alloys are listed in Table 5. For BCC and FCC structures, B/G is larger than 1.75, implying that the examined alloys are ductile [62]. A negative value of $\Gamma$ indicates a

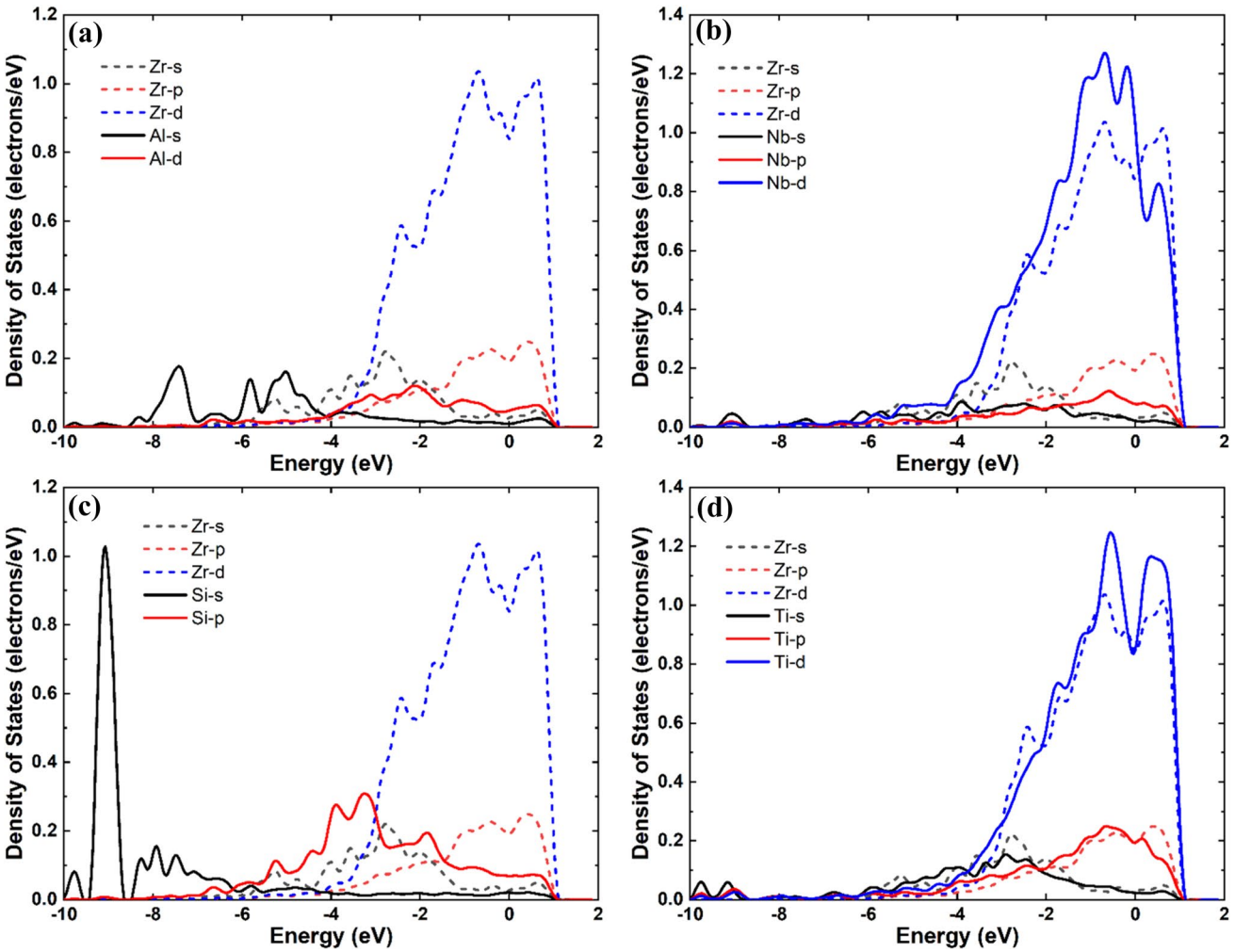


**Fig. 12** (Color online) Density of states (electrons/eV) for **a** Al, **b** Nb, **c** Si, and **d** Ti atoms in the FCC HEA/Zr interface in Fig. 2b

brittle alloy [63]. It is clear that the calculated *B*, *G*, and *E* of the Cr are significantly larger than those of the HEA coatings; thus, the Cr coating possesses better mechanical properties. With the Cr reduction and Al addition in FCC HEA and amorphous HEA alloys, the values of *B* decrease monotonously. Meanwhile, Γ decreases into negative values, and *B*/*G* becomes less than 1.75 at low Cr content. Thus, low Cr and high Al content reduce the mechanical performances and increase the brittleness of HEA coatings, providing theoretical guidance for the preparation of improved coatings.

Finally, it should be emphasized that the SQS models used in this study solely represent the possible structures of HEA coatings. SQS models with other potential distributions and different properties may also exist. However, the first-principles calculations proposed herein illuminate the comparison of Cr and HEA coating properties with different compositions, and can be used as a theoretical guide for future coating development.

This study aimed to employ theoretical calculations to discover the underlying physical mechanisms in experiments and demonstrated the utility of the combined approach of first-principles calculations and

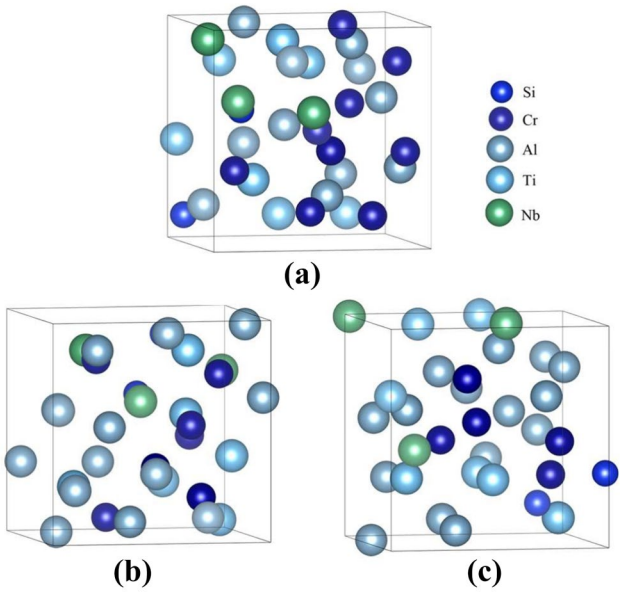


**Fig. 13** (Color online) Relaxed models of amorphous HEA alloy crystal structures: **a** Al11Cr9Nb3Si2Ti7, **b** Al13Cr7Nb3Si2Ti7, and **c** Al15Cr5Nb3Si2Ti7

experimental research for the development of new HEA coatings. Although the adhesion performance of the HEAs prepared herein is not better than that of the Cr coatings, the advantage of HEA lies in the performance-based tunability of its composition, allowing HEA coating improvement based upon elemental composition alteration. Finally, a systematic evaluation of the service performance of improved AlCrNbSiTi HEA coatings was conducted, including high-temperature electrochemistry, hydrothermal corrosion conditions, high-temperature steam oxidation [41], and fretting corrosion performance [42].

## 4 Conclusion

In this study, experimental scratch tests and first-principles calculations were used to investigate the properties of Cr and HEA coatings. The primary conclusions are summarized as follows:

(a) Cr and HEA amorphous coatings were prepared using multi-arc ion plating technology, and coating microstructure characterization was performed. The experimental results demonstrated that the Cr was well bonded while the HEA exhibited ceramic-like brittleness.

**Table 5** Calculated elastic moduli (*B*, *G*, and *E*), Pugh's ratio *B*/*G*, and Cauchy pressure (Γ) for Cr and HEA alloys. (Units in GPa.)

| Compositions | Structure | $C_{11}$ | $C_{12}$ | $C_{44}$ | *B* | *G* | *E* | *B*/*G* | Γ |
|---|---|---|---|---|---|---|---|---|---|
| Cr | BCC | 502.4 | 138.2 | 88.9 | 259.6 | 119.0 | 309.6 | 2.2 | 49.3 |
| $Al_{11}Cr_9Nb_3Si_2Ti_7$ | FCC | 123.2 | 96.7 | 66.1 | 105.6 | 35.2 | 95.1 | 3.0 | 30.6 |
| $Al_{13}Cr_7Nb_3Si_2Ti_7$ | FCC | 71.4 | 46.8 | 62.5 | 55.0 | 33.1 | 82.7 | 1.7 | −15.7 |
| $Al_{15}Cr_5Nb_3Si_2Ti_7$ | FCC | 42.8 | 20.9 | 62.5 | 28.2 | 31.8 | 69.3 | 0.9 | −41.6 |
| $Al_{11}Cr_9Nb_3Si_2Ti_7$ | Amorphous | 119.1 | 99.3 | 46.1 | 105.9 | 25.2 | 70.0 | 4.2 | 53.2 |
| $Al_{13}Cr_7Nb_3Si_2Ti_7$ | Amorphous | 125.5 | 75.3 | 47.7 | 92.0 | 36.9 | 97.5 | 2.5 | 27.6 |
| $Al_{15}Cr_5Nb_3Si_2Ti_7$ | Amorphous | 43.4 | −26.4 | 40.6 | −3.1 | 38.2 | −36.8 | −0.1 | −66.9 |

(b) First-principles calculations identified that the Cr, Nb, and Ti atoms in HEA coatings formed strong bonds with the Zr substrate, whereas Al and Si atoms do not. Low Cr and high Al content within the range of elemental concentrations examined, would reduce the mechanical performance of HEA coatings. Finally, these findings can be used as a guideline for the improvement of HEA coating development.

**Author Contributions** All authors contributed to the study conception and design. Investigation, data collection, and analysis were performed by Bao-Liang Zhang, Wen-Guan Liu, Meng-He Tu, Can Fang, and Yan Liu. Conceptualization and supervision were performed by Bao-Liang Zhang, Wen-Guan Liu, Yong Hu, and Hui Wang. The first draft of the manuscript was written by Bao-Liang Zhang and Wen-Guan Liu. And all authors commented on previous versions of the manuscript. All authors read and approved the final manuscript.

**Data Availability Statement** The data that support the findings of this study are openly available in Science Data Bank at https://cstr.cn/31253.11.sciencedb.j00186.00021 and https://doi.org/10.57760/sciencedb.j00186.00021.

## Declarations

**Conflict of interest** The authors declare that they have no conflict of interest.

## References


1. S. Bragg-Sitton, *Overview of international activities in accident tolerant fuel development for light water reactors*, in *Presentation Given at the IAEA Technical Working Group on Fuel Performance and Technology, Vienna, Austria, 24–25* (2014)
2. K.A. Terrani, Accident tolerant fuel cladding development: promise, status, and challenges. J. Nucl. Mater. **501**, 13–30 (2018). https://doi.org/10.1016/j.jnucmat.2017.12.043
3. J.C. Brachet, C. Lorrette, A. Michaux et al., *CEA studies on advanced nuclear fuel claddings for enhanced accident tolerant LWRs fuel (LOCA and beyond LOCA conditions), in Avignon, France* (2014). https://doi.org/10.13140/2.1.5105.6325
4. C.Y. Yin, S.X. Gao, S.Y. Liu et al., Transient fuel performance analysis of UO2-BeO fuel with composite SiC coated with Cr cladding based on multiphysics method. Nucl. Sci. Tech. **34**, 188 (2023). https://doi.org/10.1007/s41365-023-01344-7
5. H. Yeom, B. Maier, G. Johnson et al., High temperature oxidation and microstructural evolution of cold spray chromium coatings on Zircaloy-4 in steam environments. J. Nucl. Mater. **506**, 151737 (2019). https://doi.org/10.1016/j.jnucmat.2019.151737
6. T. Wei, R. Zhang, H. Yang et al., Microstructure, corrosion resistance and oxidation behavior of Cr-coatings on Zircaloy-4 prepared by vacuum arc plasma deposition. Corros. Sci. **158**, 108077 (2019). https://doi.org/10.1016/j.corsci.2019.06.029
7. J. Bischoff, C. Delafoy, C. Vauglin et al., AREVA NP's enhanced accident-tolerant fuel developments: focus on Cr-coated M5 cladding. Nucl. Eng. Technol. **50**, 223–228 (2018). https://doi.org/10.1016/j.net.2017.12.004
8. H.G. Kim, I.H. Kim, Y.I. Jung et al., Adhesion property and high-temperature oxidation behavior of Cr-coated Zircaloy-4 cladding tube prepared by 3D laser coating. J. Nucl. Mater. **465**, 531–539 (2015). https://doi.org/10.1016/j.jnucmat.2015.06.030
9. W. Zhong, P.A. Mouche, B.J. Heuser, Response of Cr and Cr–Al coatings on Zircaloy-2 to high temperature steam. J. Nucl. Mater. **498**, 137–148 (2018). https://doi.org/10.1016/j.jnucmat.2017.10.021
10. X. Li, C. Meng, X. Xu et al., Effect of Al content on high-temperature oxidation behavior and failure mechanism of CrAl-coated Zircaloy. Corros. Sci. **192**, 109856 (2021). https://doi.org/10.1016/j.corsci.2021.109856
11. X. He, H. Zhan, J. Lin et al., Effect of Si content of CrSi-based coatings on their oxidation resistance in high temperature air. Ceram. Int. **46**, 11357–11363 (2020). https://doi.org/10.1016/j.ceramint.2020.01.165
12. W. Zhong, P.A. Mouche, X. Han et al., Performance of iron-chromium-aluminum alloy surface coatings on Zircaloy 2 under high-temperature steam and normal BWR operating conditions. J. Nucl. Mater. **470**, 327–338 (2016). https://doi.org/10.1016/j.jnucmat.2015.11.037
13. Z. Duan, P. Chen, Y. Zhou et al., Current progress of Cr-coated zirconium alloy cladding for accident tolerant fuel. Nucl. Tech. **45**, 030001 (2022). https://doi.org/10.11889/j.0253-3219.2022.hjs.45.030001
14. J. Jiang, M. Du, Z. Pan et al., Effects of oxidation and inter-diffusion on the fracture mechanisms of Cr-coated Zry-4 alloys: an in situ three-point bending study. Mater. Des. **212**, 110168 (2021). https://doi.org/10.1016/j.matdes.2021.110168
15. J. Yang, U. Stegmaier, C. Tang et al., High temperature Cr-Zr interaction of two types of Cr-coated Zr alloys in inert gas environment. J. Nucl. Mater. **547**, 152806 (2021). https://doi.org/10.1016/j.jnucmat.2021.152806
16. X. Han, J. Xue, S. Peng et al., An interesting oxidation phenomenon of Cr coatings on Zry-4 substrates in high temperature steam environment. Corros. Sci. **156**, 117–124 (2019). https://doi.org/10.1016/j.corsci.2019.05.017
17. J.W. Yeh, S.K. Chen, S.J. Lin et al., Nanostructured high-entropy alloys with multiple principal elements: novel alloy design concepts and outcomes. Adv. Eng. Mater. **6**, 299–303 (2004). https://doi.org/10.1002/adem.200300567
18. T. Li, Y. Lu, Z. Cao et al., Opportunity and challenge of refractory high-entropy alloys in the field of reactor structural materials. Acta Metall. Sin. **57**, 42–54 (2021). https://doi.org/10.11900/0412.1961.2020.00293
19. T. Li, S. Wang, W. Fan et al., CALPHAD-aided design for superior thermal stability and mechanical behavior in a TiZrHfNb refractory high-entropy alloy. Acta Mater. **246**, 118728 (2023). https://doi.org/10.1016/j.actamat.2023.118728
20. T. Li, W. Jiao, J. Miao et al., A novel ZrNbMoTaW refractory high-entropy alloy with in-situ formingheterogeneous structure. Mat. Sci. Eng. A **827**, 142061 (2021).https://doi.org/10.1016/j.msea.2021.142061
21. T. Li, Y. Lu, Z. Li et al., Hot deformation behavior and microstructure evolution of non-equimolar $Ti_2$ $ZrHfV_{0.5}$ $Ta_{0.2}$ refractory high-entropy alloy. Intermetallics **146**, 107586 (2022). https://doi.org/10.1016/j.intermet.2022.107586
22. M. Wang, Y. Lu, J. Lan et al., Lightweight, ultrastrong and high thermal-stable eutectic high-entropy alloys for elevated-temperature applications. Acta Mater. **248**, 118806 (2023). https://doi.org/10.1016/j.actamat.2023.118806
23. Q. Wu, F. He, J. Li et al., Phase-selective recrystallization makes eutectic high-entropy alloys ultra-ductile. Nat. Commun. **13**, 4697 (2022). https://doi.org/10.1038/s41467-022-32444-4
24. J. Ren, Y. Zhang, D. Zhao et al., Strong yet ductile nanolamellar high-entropy alloys by additive manufacturing. Nature **608**, 62–68 (2022). https://doi.org/10.1038/s41586-022-04914-8
25. H. Guan, L. Chai, Y. Wang et al., Microstructure and hardness of NbTiZr and NbTaTiZr refractory medium-entropy alloy coatings

on Zr alloy by laser cladding. Appl. Surf. Sci. **549**, 149338 (2021). https://doi.org/10.1016/j.apsusc.2021.149338
26. L. Chai, C. Wang, K. Xiang et al., Phase constitution, microstructure and properties of pulsed laser-clad ternary CrNiTi medium-entropy alloy coating on pure titanium. Surf. Coat. Tech. **402**, 126503 (2020). https://doi.org/10.1016/j.surfcoat.2020.126503
27. K. Xiang, L. Chai, C. Zhang et al., Investigation of microstructure and wear resistance of laser-clad CoCrNiTi and CrFeNiTi medium-entropy alloy coatings on Ti sheet. Opt. Laser Technol. **145**, 107518 (2022). https://doi.org/10.1016/j.optlastec.2021.107518
28. M. Zhang, X. Zhou, X. Yu et al., Synthesis and characterization of refractory TiZrNbWMo high-entropy alloy coating by laser cladding. Surf. Coat. Tech. **311**, 321–329 (2017). https://doi.org/10.1016/j.surfcoat.2017.01.012
29. K. Feng, Y. Zhang, Z. Li et al., Corrosion properties of laser cladded CrCoNi medium entropy alloy coating. Surf. Coat. Tech. **397**, 126004 (2020). https://doi.org/10.1016/j.surfcoat.2020.126004
30. H. Xin, J. Yang, J. Mao et al., Effect of Al concentration on microstructure and properties of AlNbTiZr medium-entropy alloy coatings. Materials **14**, 7661 (2021). https://doi.org/10.3390/ma14247661
31. H. Cui, D. Jiang, Research progress of high-entropy alloy coatings. Acta Metall. Sin. **58**, 17–27 (2021). https://doi.org/10.11900/0412.1961.2021.00193
32. G.J. Zhang, Q.W. Tian, K.X. Yin et al., Effect of Fe on microstructure and properties of AlCoCrFexNi (x= 1.5, 2.5) high entropy alloy coatings prepared by laser cladding. Intermetallics **119**, 106722 (2020). https://doi.org/10.1016/j.intermet.2020.106722
33. H. Liu, T. Zhang, S. Sun et al., Microstructure and dislocation density of AlCoCrFeNiSix high entropy alloy coatings by laser cladding. Mater. Lett. **283**, 128746 (2021). https://doi.org/10.1016/j.matlet.2020.128746
34. B.S. Lou, F.R. Kan, W. Diyatmika et al., Property evaluation of TixZrNbTaFeBy high entropy alloy coatings: effect of Ti and B contents. Surf. Coat. Tech. **434**, 128180 (2022). https://doi.org/10.1016/j.surfcoat.2022.128180
35. H. Xin, J. Yang, W. Zhang et al., Effect of Au ion irradiation on the surface morphology, microstructure and mechanical properties of AlNbTiZr medium-entropy alloy coatings with various Al content for ATF. Surf. Coat. Tech. **434**, 128157 (2022). https://doi.org/10.1016/j.surfcoat.2022.128157
36. W. Zhang, R. Tang, Z.B. Yang et al., Preparation, structure, and properties of an AlCrMoNbZr high-entropy alloy coating for accident-tolerant fuel cladding. Surf. Coat. Tech. **347**, 13–19 (2018). https://doi.org/10.1016/j.surfcoat.2018.04.037
37. W. Zhang, R. Tang, Z.B. Yang et al., Preparation, structure, and properties of high-entropy alloy multilayer coatings for nuclear fuel cladding: a case study of AlCrMoNbZr/(AlCrMoNbZr)N. J. Nucl. Mater. **512**, 15–24 (2018). https://doi.org/10.1016/j.jnucmat.2018.10.001
38. W. Zhang, M. Wang, L. Wang et al., Interface stability, mechanical and corrosion properties of AlCrMoNbZr/(AlCrMoNbZr) N high-entropy alloy multilayer coatings under helium ion irradiation. Appl. Surf. Sci. **485**, 108–118 (2019). https://doi.org/10.1016/j.apsusc.2019.04.192
39. Y. Li, F. Meng, F. Ge et al., Improved oxidation resistance through an in-situ formed diffusion barrier: oxidation behavior of amorphous multi-component FeCrAlMoSiY-coated Zr in high-temperature steam. Corros. Sci. **189**, 109566 (2021). https://doi.org/10.1016/j.corsci.2021.109566
40. Y. Li, F. Meng, P. Li et al., Xe20+ ions irradiation and autoclave corrosion coupled with steam oxidation behaviors of FeCrAlMoSiY-coated Zr claddings. Surf. Coat. Tech. **433**, 128166 (2022). https://doi.org/10.1016/j.surfcoat.2022.128166
41. M. Tu, Y. Hu, B. Zhang et al., Protection of AlCrNbSiTi high entropy alloy coating on zirconium alloy by high-temperature steam oxidation at 1200 °C. Atom. Energy Sci. Technol. **57**, 1606–1613 (2023). (in Chinese)
42. X. Liu, S. Li, H. Wang et al., Fretting corrosion performance evaluation of uncoated cladding, Cr coating cladding and AlCrNbSiTi coating cladding. Alloys **2**, 227–241 (2023). https://doi.org/10.3390/alloys2040016
43. J. Hui, B. Zhang, T. Liu et al., Effects of impurity elements on SiC grain boundary stability and corrosion. Nucl. Sci. Tech. **32**, 125 (2021). https://doi.org/10.1007/s41365-021-00963-2
44. T. Liu, J. Hui, B. Zhang et al., Corrosion mechanism of lead-bismuth eutectic at grain boundary in ferritic steels and the effect of alloying elements: a first-principles study. J. Nucl. Mater. **569**, 153915 (2022). https://doi.org/10.1016/j.jnucmat.2022.153915
45. J. Li, L. Dong, X. Dong et al., Study on wear behavior of FeNiCr-CoCu high entropy alloy coating on Cu substrate based on molecular dynamics. Appl. Surf. Sci. **570**, 151236 (2021). https://doi.org/10.1016/j.apsusc.2021.151236
46. T. Liu, B. Zhang, H. Yin et al., First-principles study on the corrosion resistance of iron oxide surface and grain boundary in austenitic steel to lead-bismuth eutectic. Appl. Surf. Sci. **640**, 158409 (2023). https://doi.org/10.1016/j.apsusc.2023.158409
47. S. Yang, R. Fang, G. Yang et al., Influence of element substitutions on poisoning behavior of ZrV2 alloy: theoretical and experimental investigations. Nucl. Sci. Tech. **34**, 113 (2023). https://doi.org/10.1007/s41365-023-01259-3
48. A. Zunger, S.H. Wei, L.G. Ferreira et al., Special quasirandom structures. Phys. Rev. Lett. **65**, 353 (1990). https://doi.org/10.1103/PhysRevLett.65.353
49. A. Van De Walle, M. Asta, G. Ceder, The alloy theoretic automated toolkit: a user guide. Calphad **26**, 539–553 (2002). https://doi.org/10.1016/S0364-5916(02)80006-2
50. F. Mouhat, F.X. Coudert, Necessary and sufficient elastic stability conditions in various crystal systems. Phys. Rev. B **90**, 224104 (2014). https://doi.org/10.1103/PhysRevB.90.224104
51. G. Kresse, J. Furthmüller, Efficient iterative schemes for ab initio total-energy calculations using a plane-wave basis set. Phys. Rev. B **54**, 11169 (1996). https://doi.org/10.1103/PhysRevB.54.11169
52. P. Hohenberg, W. Kohn, Inhomogeneous electron gas. Phys. Rev. **136**, B864 (1964). https://doi.org/10.1103/PhysRev.136.B864
53. W. Kohn, L.J. Sham, Self-consistent equations including exchange and correlation effects. Phys. Rev. **140**, A1133 (1965). https://doi.org/10.1103/PhysRev.140.A1133
54. P.E. Blöchl, Projector augmented-wave method. Phys. Rev. B **50**, 17953 (1994). https://doi.org/10.1103/PhysRevB.50.17953
55. J.P. Perdew, J.A. Chevary, S.H. Vosko et al., Atoms, molecules, solids, and surfaces: applications of the generalized gradient approximation for exchange and correlation. Phys. Rev. B **46**, 6671 (1992). https://doi.org/10.1103/PhysRevB.46.6671
56. D. Di Stefano, M. Mrovec, C. Elsässer, First-principles investigation of hydrogen trapping and diffusion at grain boundaries in nickel. Acta Mater. **98**, 306–312 (2015). https://doi.org/10.1016/j.actamat.2015.07.031
57. X. He, Z. Tian, B. Shi et al., Effect of gas pressure and bias potential on oxidation resistance of Cr coatings. Ann. Nucl. Energy **132**, 243–248 (2019). https://doi.org/10.1016/j.anucene.2019.04.038
58. Y.N. Smirnov, V.A. Finkel, Crystal structure of chromium at 113–373 degrees k. Sov. Phys. J. **20**, 315 (1965)
59. R.M.C. Gao, J.W. Yeh, P.K. Liaw et al., *High-Entropy Alloys: Fundamentals and Applications* (Springer, Berlin, 2016)
60. L. Vitos, *Computational Quantum Mechanics for Materials Engineers: the EMTO Method and Applications* (Springer, Berlin, 2007)
61. M.C. Gao, Ö.N. Doğan, P. King et al., The first-principles design of ductile refractory alloys. JOM **60**, 61–65 (2008). https://doi.org/10.1007/s11837-008-0092-1
62. Z. Huang, G. Liu, B. Zhang et al., A theoretical study of the stability, mechanical and thermal properties of AlNiCuCo equimolar high

entropy alloy. Phys. Lett. A **384**, 126797 (2020). https://doi.org/10.1016/j.physleta.2020.126797
63. D. Nguyen-Manh, M. Mrovec, S.P. Fitzgerald, Dislocation driven problems in atomistic modelling of materials. Mater. Trans. **49**, 2497–2506 (2008). https://doi.org/10.2320/matertrans.MB200827